



Experimental Investigation of a 64 Ah Lithium-Ion Pouch Cell

Hamid Hamed,^{1,2,3} Behnam Ghalami Choobar,¹ Sarallah Hamtaei,^{1,2,3} Jan D'Haen,^{1,3}
Bart Vermang,^{1,2,3} and Mohammadhosein Safari^{1,2,3,z} 

¹Institute for Materials Research (IMO-imomec), UHasselt, B-3500 Hasselt, Belgium

²Energyville, Thor Park 8320, Genk B-3600, Belgium

³IMEC division IMOMEc, Diepenbeek BE-3590, Belgium

This study presents a meticulous investigation and characterization of a 64 Ah commercial lithium-ion pouch cell. Notably, an exhaustive analysis of the cell's open-circuit voltage and kinetics attributes is conducted, with particular emphasis on the temperature-dependent dynamics. Subsequently, a teardown experiment is performed, offering an incisive insight into the macrogeometrical properties underpinning the cell's architecture. Further details about the microstructural features and formulation inherent to the cathode and anode are revealed after image processing of the electrodes' cross sections. The details of cell balancing and cycling window of the electrodes in the pouch cell are determined and discussed based on the open-circuit-voltage measurements of the individual electrodes and a simple optimization algorithm. The methodologies presented in this work are insightful on the characterization and model parametrization of the high-capacity commercial lithium-ion cells.

© 2024 The Author(s). Published on behalf of The Electrochemical Society by IOP Publishing Limited. This is an open access article distributed under the terms of the Creative Commons Attribution 4.0 License (CC BY, <http://creativecommons.org/licenses/by/4.0/>), which permits unrestricted reuse of the work in any medium, provided the original work is properly cited. [DOI: 10.1149/1945-7111/ad24c2]



Manuscript submitted October 26, 2023; revised manuscript received December 28, 2023. Published February 9, 2024.

Lithium-ion cells with different chemistries, shape formats, and sizes are used over a broad range of applications from portable electronics and electric vehicles to grid storage.^{1,2} In these applications, the architectural complexity, synergistic interactions among the different components, and the capacity of the cells are much larger compared to those of the small coin cells popular in the research labs. This disparity complicates the direct translation of the individual components' properties and performance, obtained from the experimentation and modeling on the coin cells, to the commercial cells.

Commercial lithium-ion cells consist of multiple layers of cathodes, anodes, and separators that are infused with the electrolyte. These layers can be organized in various arrangements, such as discrete layers of electrodes placed atop one another with a zigzag pattern of a continuous roll of separator in between within a pouch cell enclosure, or the continuous rolls of electrodes and separators wound into a cylindrical shape.³ A comprehensive understanding of the internal parameters of the commercial cells and their evolution during service life enables the design of accurate battery management systems and facilitates the recycling and repurposing of the cells for second life applications. In contrast to the half-cell investigations, only a limited number of in-depth studies on the commercial large lithium-ion cells are available in the literature.^{4,5} This gap in research hinders the effective utilization of findings for modeling, algorithm design, and validation.

Quantitative investigation of the lithium-ion batteries' performance can be facilitated using battery models. Notably, sophisticated physics-centered models such as the Doyle-Fuller-Newman are being used for more than two decades to emulate the performance of lithium-ion batteries under various operational circumstances.^{6,7} These models are employed to discern the attributes of different components of the cell and to determine the internal parameters such as kinetics and transport properties of the electrodes and electrolyte. This is achieved by aligning the model's simulation results with measurable battery performance indicators such as terminal voltage, current, and temperature. The parametrization of such models is usually facilitated by numerous sensitivity analyses and parameter estimation techniques rooted in statistical principles.^{8–10} Noteworthy is the application of the specific electrochemical test protocols such as GITT to the half-cells to isolate certain physics and determine the corresponding parameters.^{11,12}

Although model parameterization methods have displayed encouraging outcomes for lithium-ion batteries, the reports on the parameterization of the commercial cells are limited in the literature.¹³ This particularly hinders the progress in applications that exhibit heightened sensitivity to the cell parameters such as state of charge and health estimation.¹⁴ In light of these considerations, the added value of the cell teardown experiments becomes significantly valuable to develop accurate models of the full cells. Such experiments offer the capacity to gain deep quantitative insights into the (electro)chemical and microstructural details of the individual components and the important design parameters like stack architecture and cell balancing.

In this study, a commercial 64 Ah lithium-ion pouch cell is characterized and dismantled for a comprehensive analysis of the electrodes and cell design parameters. This battery cell has been engineered for high energy applications such as waterborne transport. First, the open circuit voltage (OCV), voltage recovery during the pulse-relaxation test, and the rate capability of the full cell is measured. Next, the cell is opened and the individual electrodes are recovered to perform a series of (electro)chemical and microstructural analyses. Finally, the balancing of the cell is determined by reconstructing the OCV of the full cell from the individual OCVs of the cathode and anode electrodes.

Experiments and Methods

In this study, a lithium-ion pouch cell with a nominal capacity of $64 \pm 2.5\%$ Ah is investigated. The cell weighs 1156.2 grams and has dimensions of approximately $100.2 \pm 1.5 \times 352.5 \pm 1 \times 16.1 \pm 0.1$ mm. The positive and negative terminal tabs are situated on opposite sides of the pouch cell, along its longest dimension. The electrochemical characterizations of the pouch cell were performed using a NEWARE CT-8008–5V60A-NTFA battery cycler. The pouch cells were cycled at isothermal conditions inside an explosion-proof temperature chamber (Espec-LU114). The pouch cells were opened inside an Ar-filled glovebox and the electrodes were recovered for further (electro)chemical investigations. After opening the cell, 15 mm disk samples were punched from the cathode and anode electrode sheets. These samples were then thoroughly washed with dimethyl carbonate (DMC) and left to dry for 24 h. The coating layers from one side of the electrodes were removed by wiping the samples with NMP and very fine sandpapers inside the glovebox. The electrode disks were then taken outside for a thorough drying process at 110 °C overnight. Once the drying was completed, the electrodes were transferred back into the glove box for assembly of

^zE-mail: momo.safari@uhasselt.be

the half-cells with a counter Li electrode. Prior to the assembly, the weight of the electrodes was carefully measured to calculate the capacity and C-rate. The standard 2025 coin-cell format was used with 1 M LiPF₆ in EC/EMC as the electrolyte. All cells were tested using the Bio-Logic BCS-815 cycler. The cells were left at rest for 24 h before the formation cycles, i.e. three (dis)charge cycles at C/10. The upper and lower cutoff voltage limits were set to 4.3 V and 3.0 V for the cathode half-cell and 2 V and 0.005 V for the anode half-cell, respectively. The morphology and elemental analysis of the electrodes were investigated by a scanning electron microscope (FEI Quanta 200 F) equipped with energy dispersive X-ray analysis (EDX).

Results and Discussion

Open-circuit-voltage (OCV).—The OCV and the precise capacity of the pouch cell was measured following the approach proposed by G.L.Plett.¹⁵ This protocol consists of five distinct test scripts conducted at 25 °C:

Script #1. In this step, the cell is brought to its fully discharged state using a CCCV protocol, i.e. a constant-current (CC) followed by a constant-voltage (CV) step. The CC discharge is performed at C/20 and the CV step uses the C/50 current as the stop condition. The cell is then allowed to rest for at least two hours.

Script #2. This step involves a low rate (C/50) constant current charge until the upper voltage cutoff is reached (4.2 V).

Script #3. A CV step at the upper voltage cutoff until the current is lower than C/100, followed by a rest period for at least two hours.

Script #4. This step involves a low rate (C/50) CC discharge until the lower voltage cutoff is reached (3 V).

Script #5. A CV step at the lower voltage cutoff until the current is lower than C/100.

The raw data from the OCV measurement (Fig. 1a) needs further processing to obtain the OCV as a function of the state-of-charge (SOC) of the cell (Fig. 1b). In summary, the coulomb counting is used to separately define the SOC coordinates for the charge (script #2) and discharge (script #4) steps based on the lithiation state of the anode. This means that at SOC=0, the lithiation states at the anode and cathode electrodes are minimum and maximum, respectively. In this regard, the SOC at the end of script #3 and script #1 is 1 and 0, respectively. The cell voltage at the end of script #3 and script #1 differs from the upper and lower voltage cutoff limits (Fig. 1a). This leads to a missing data issue at the extreme ends of the SOC range (0 and 1). At the proximity of SOC = 0 and SOC = 1 the discharge and charge OCV tails, respectively, are incomplete (inset Fig. 1b). To solve this problem, following the work of Plett¹⁵ the charge and discharge OCV curves are fitted with a very smoothed function and

extrapolated into the missing ranges. Next, the final OCV is obtained by averaging the charge and discharge OCV voltages (black line in Fig. 1b). This method is referred to as the “voltage averaging” method of which more details can be consulted in the works of Plett and Lu et al.^{15,16}

Resistance and rate capability.—A pulse-relaxation test was performed at 15, 25, and 35 °C to investigate the internal resistance of the pouch cell and its sensitivity to the temperature and SOC (Fig. 2a). In this test, starting from a fully charged cell, a discharge CC pulse at 0.2 C is applied for a duration of 10 min and then the current is interrupted for a sufficient amount of time until the voltage changes are relatively insignificant. In this test, the voltage recovery immediately after the current interruption is investigated to estimate the ohmic and non-ohmic internal resistance of the pouch cell (inset Fig. 2a). The ohmic resistance is defined based on the instantaneous relaxation of voltage, i.e., the change of voltage 100 ms after the current interruption, ΔV_{ohmic} . The non-ohmic resistance is defined based on the long-term (100 ms < $t < t_{\infty}$) recovery of voltage ($\Delta V_{non-ohmic}$) with t_{∞} being the time after which the rate of voltage change is less than 0.1 mV s⁻¹. The ohmic (R_o) and non-ohmic (R_{no}) resistances are calculated based on the following equations:

$$R_o = \frac{|\Delta V_{ohmic}|}{I} \quad [1]$$

$$R_{no} = \frac{|\Delta V_{non-ohmic}|}{I} \quad [2]$$

where, I is the current during the pulse period. The R_o is higher at lower SOC at all temperatures (Fig. 2b). This might be explained by the SOC dependence of the electronic conductivity at the cathode. The identity of the anode and cathode active materials will be later shown to be graphite and NMC, respectively. It is known that the electronic conductivity of the NMC family of cathode materials is lower at higher lithiation states.¹⁷ Therefore, at low SOC of the pouch cell where the cathode material approaches its fully lithiated state, the poorer electronic conductivity of the cathode can increase the ohmic resistance of the cell. The ohmic resistance, however, displays a substantial correlation with temperature, demonstrating an escalating trend as the temperature decreases (Fig. 2b). This observation might stem from the higher ionic conductivity of the electrolyte at higher temperatures. Such a temperature sensitivity is expected for the typical carbonate based electrolytes that are widely used in commercial lithium-ion cells.^{18,19} The temperature sensitivity of R_o can be used to determine a lumped activation energy using the following equation

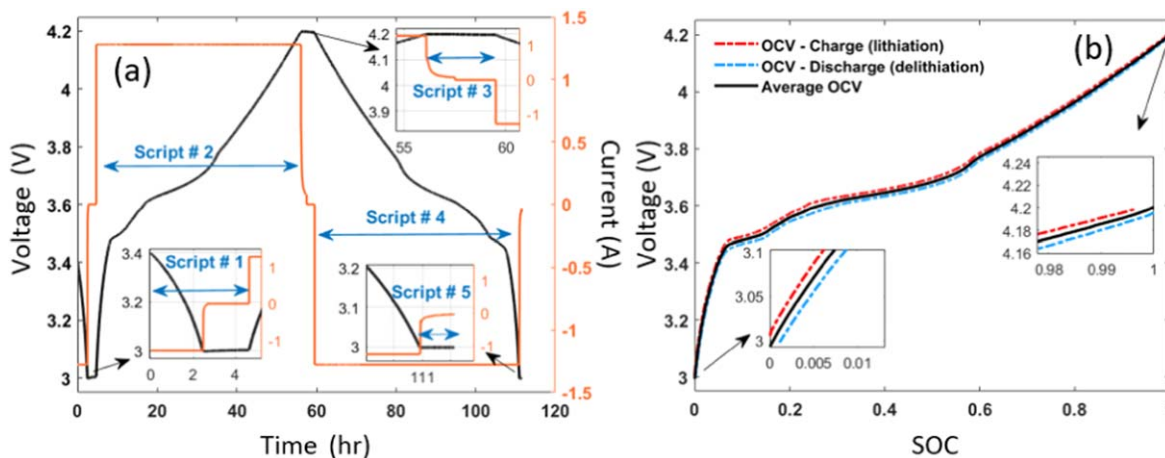


Figure 1. (a) the unprocessed OCV data of the pouch cell obtained from the OCV test protocol outlined in the text. (b) the processed charge and discharge OCV data and the average OCV data as a function of SOC.

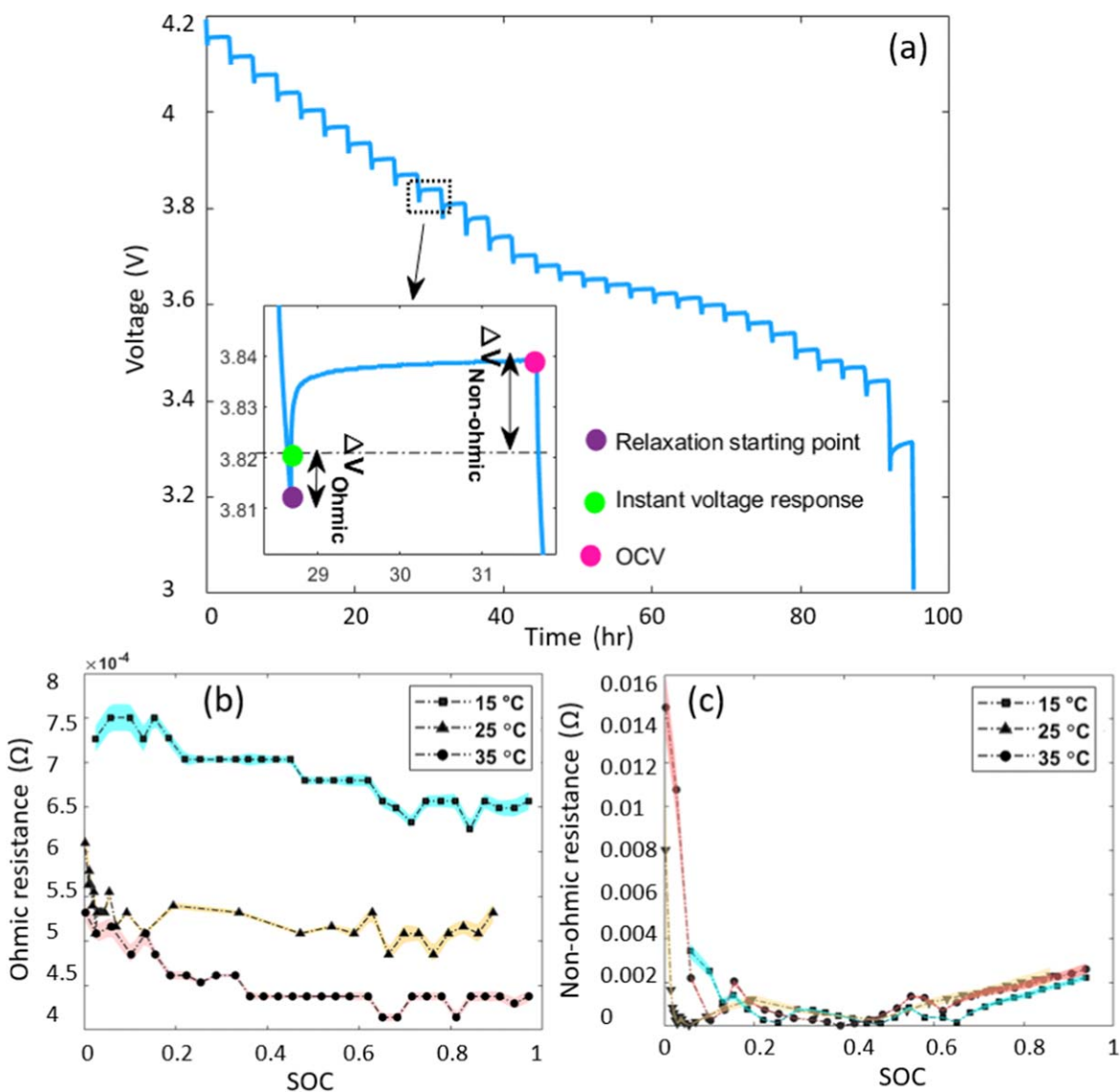


Figure 2. (a) pulse-relaxation test performed on a fully charged pouch cell. 0.2 C current pulses were applied for 10 min and then the current was interrupted. The ΔV_{Ohmic} and $\Delta V_{Non-Ohmic}$ shown in the inset were used to estimate the ohmic and non-ohmic resistances. (b) The ohmic (R_o) and (c) non-ohmic (R_{no}) resistances as function of SOC and temperature. The shaded region in (b) and (c) subplots represent the level of uncertainty associated with the measurements. The measurements were repeated two times on two identical cells.

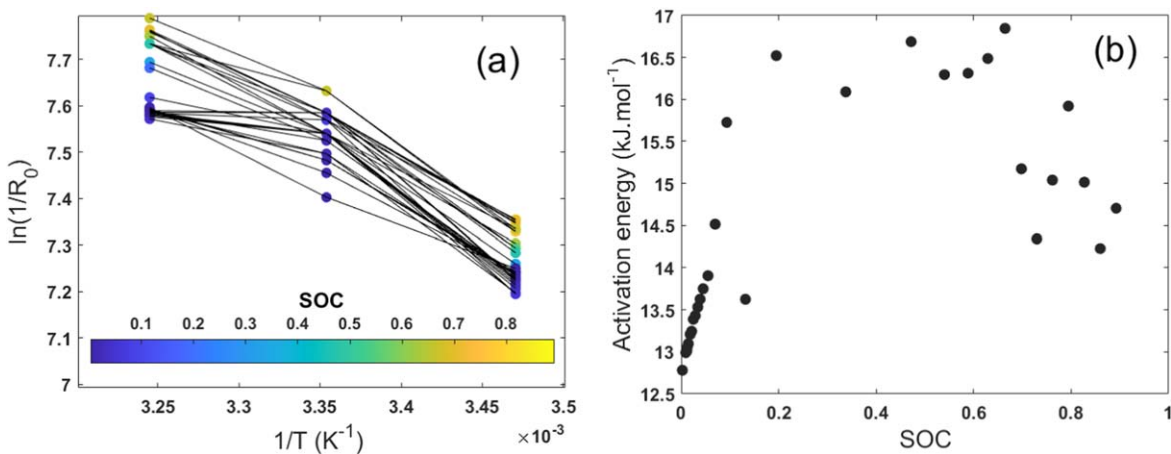


Figure 3. (a) Variation of the ohmic resistance of the pouch cell (R_o) with temperature. The R_o values corresponding to the same SOC are connected with a line, (b) the activation energy as a function of SOC for the temperature sensitivity of the R_o derived based on Eq. 3.

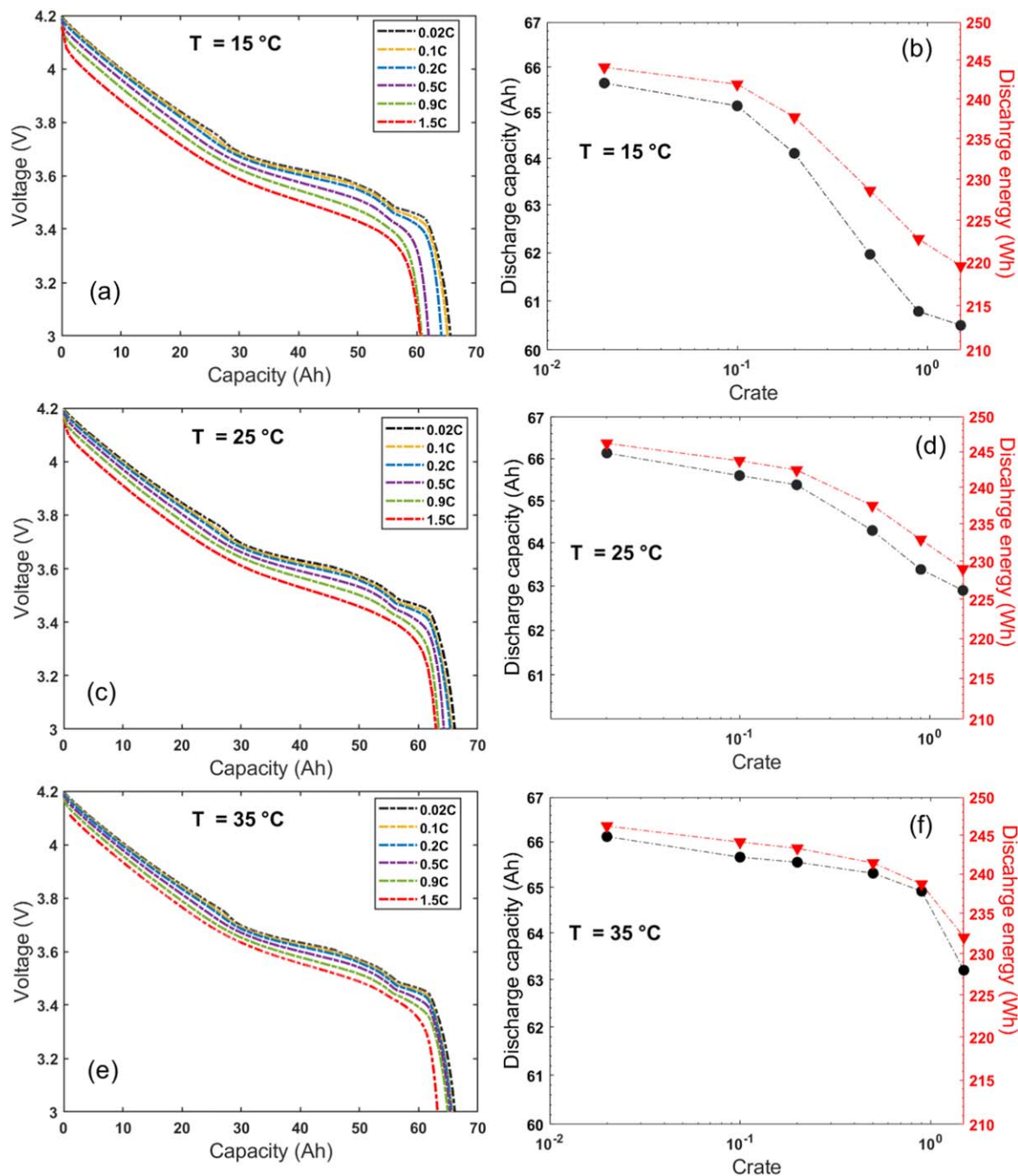


Figure 4. The CC discharge profiles of the pouch cell at different C-rates at (a) 15 °C, (c) 25 °C, and (e) 35 °C. The discharge capacity and discharge energy of the pouch cell as a function of C-rate at (b) 15 °C, (d) 25 °C, and (f) 35 °C.

$$\frac{1}{R_o} = A_0 \exp\left(-\frac{E_a}{RT}\right) \quad [3]$$

where, A_0 is a fitting parameter, R is the gas constant, and E_a is the activation energy. The activation energy has an average value of 14.5 kJ mol^{-1} and is SOC dependent (Fig. 3). This E_a value is similar to those reported for the most common commercial liquid electrolytes in lithium-ion batteries.^{13,14} For instance, Logan et al.²⁰ report an activation energy of 7 kJ mol^{-1} for the ionic conductivity of the 1 mol kg^{-1} LiPF_6 in ethylene carbonate + ethyl methyl carbonate (EC:EMC 30:70 (wt%)).

It is noteworthy that the choice of 100 ms as a threshold to distinguish between the ohmic and non-ohmic contributions to the cell

polarization was mainly governed by the sampling rate limitation of the battery cycler. The very high sampling rates are ideal to avoid the interference of lower frequency phenomena such as diffusion with the ohmic effects. Moreover, the amplitude and duration of the pulse are adjustable parameters that can impact the obtained resistance values. As such, an additional comparable pulse-relaxation test at 25 °C was conducted using a different amplitude of 0.8 C. The ohmic resistance was computed after a 100 ms pause in the current flow (refer to Fig. A-2). The resulting ohmic resistance values based on the 0.8 C pulses fall in the same range as those earlier obtained with 0.2 C pulses (Fig. 2b). This observation indicates that 100 ms is good enough to capture the ohmic resistance of the cell subject to the current range and duration of the pulses used in this study. The pulse-relaxation protocol, however, is not as rich as the electrochemical

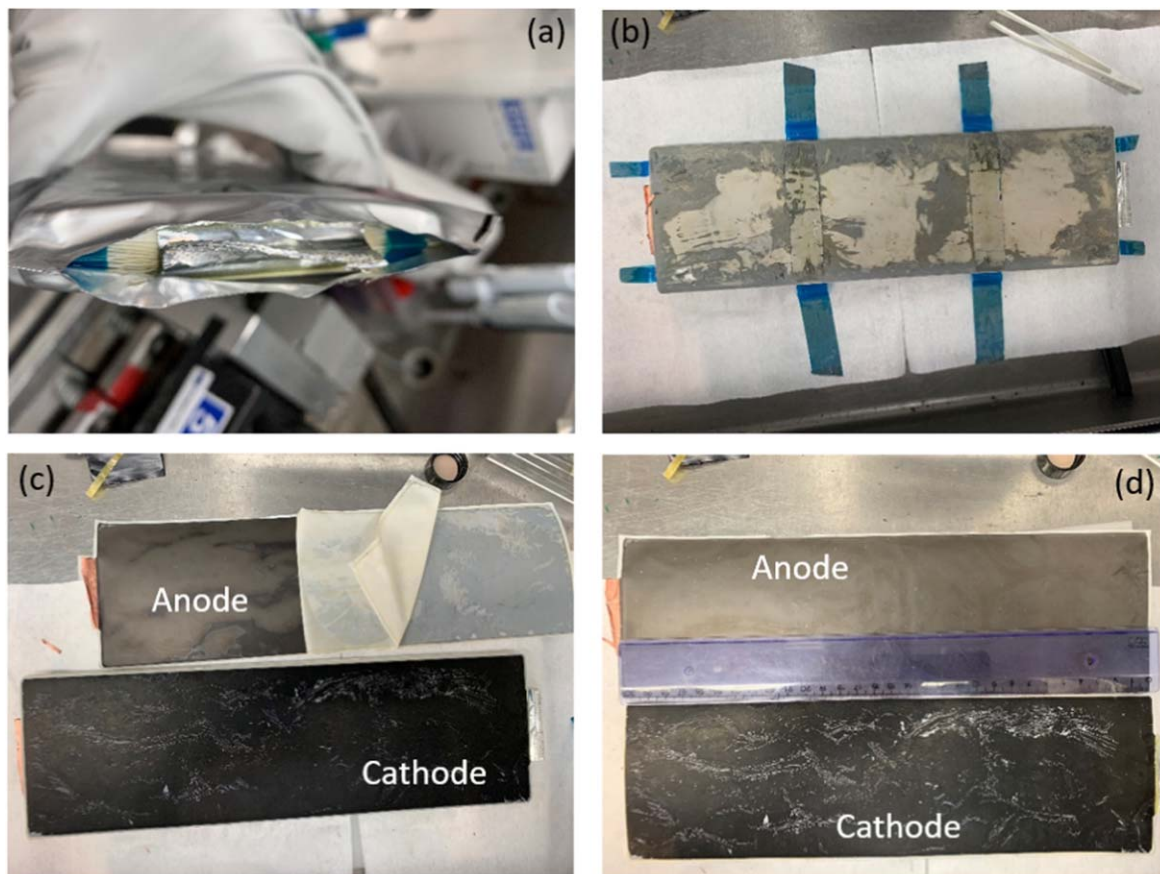


Figure 5. (a) Few representative snapshots from the teardown process of the pouch cell. The cell was opened near the tab using a ceramic scissor. The unwrapped cell components are shown in (b) after the cell casing was removed. (c) the separation of the cathode and anode layers. (d) Recovered anode and cathode sheets next to a 30 cm ruler.

impedance spectroscopy (EIS) where the cell impedance can be readily recorded as a function of the frequency.

The R_{no} demonstrates a weak dependence on the temperature compared to the R_o (Fig. 2c). Noteworthy are the strikingly higher values of R_{no} at SOC near 0 and 1 which is in line with the previous reports on similar cell chemistries.²¹ The non-ohmic resistance originates from a combination of various phenomena including the charge-transfer at electrode/electrolyte interface and charge transport within the electrolyte as well as the solid-state diffusion of lithium within the active-material particles of the anode and cathode.^{22,23} Particularly, the charge-transfer resistance is very sensitive to the slope of OCV ($\frac{\partial U}{\partial SOC}$) and the SOC of the cathode and anode. In this regard, the polarization considerably increases at the extreme values of SOC for the common active-materials such as graphite and NMC near the completely delithiated and lithiated states, respectively.²⁴

The rate capability of the pouch cell was determined at different temperatures (Fig. 4). The cell was CC discharged at five C-rates of 0.02 C, 0.1 C, 0.2 C, 0.5 C, 0.9 C, and 1.5 C starting from a fully charged cell at three different temperatures of 15, 25, and 35 °C. The discharge capacity and energy of the cell is summarized in Figs. 4b, 4d, 4f as a function of C-rate and temperature. The polarization increases at higher C-rates at all temperatures, but with the largest sensitivity at 15 °C (Figs. 4a, 4c, 4e). The higher C-rate sensitivity of the cell discharge capacity at lower temperatures is in-line with the higher ohmic resistance at lower temperature observed earlier (Fig. 2b). This suggests that the cell performance is mainly limited by the ohmic-resistance in the range of C-rate considered in this study.

Cell teardown.—The cell was dismantled after a deep discharge with a constant-current (CC) constant-voltage (CV) protocol. The

cell was first CC discharged at C/10 until it reached the lower cutoff voltage of 3 V after which a CV step was applied with a cutoff current of 1.28 A corresponding to the C-rate of C/50. The cell was left to rest for 24 h before entry to the glovebox. Inside the Ar-filled glovebox, the cell was opened using a ceramic scissor to minimize the chance of short circuit. The initial step involved making a cut around one of the terminal tabs, followed by unwrapping the remaining cell casing (Fig. 5a). Next, the stack was taken out from its packaging, and the adhesive strips were loosened (Fig. 5b). The stack is composed of 52 layers of cathode and 53 layers of anode (Fig. 5c). The cathode sheets measure 302 × 90 mm, while the anode sheets measure 305 × 93 mm (Fig. 5d). Each electrode sheet was carefully recovered from the stack and stored separately inside the glovebox for further investigations. The coating thickness on a single-side of the anode and cathode is 58 μm and 49 μm, respectively (Mitutoya digital micrometer with a precision of 0.1 μm), corresponding to the loading densities of 7.92 mg cm⁻² and 15.1 mg cm⁻² at the anode and cathode, respectively.

Morphological analysis.—The scanning electron microscope (SEM) images of the surface of the cathode, anode, and separator are shown in Fig. 6. The EDX data of the cathode surface show that the cathode active material is composed of nickel, manganese and cobalt. The XRD measurement on the cathode revealed that the composition of the cathode active material is Ni_{0.33}Mn_{0.33}Co_{0.33} (see appendix, Fig. A-1, Table A-1). The EDX result of the anode shows that the active material of the anode is graphite. The surface of both electrodes is partially covered by a distinct bright cloud-like feature. The EDX analysis of these specific regions points out to the presence of aluminum. The aluminum signal is speculated to stem from a thin Al₂O₃ layer on the separator's surface. This Al₂O₃

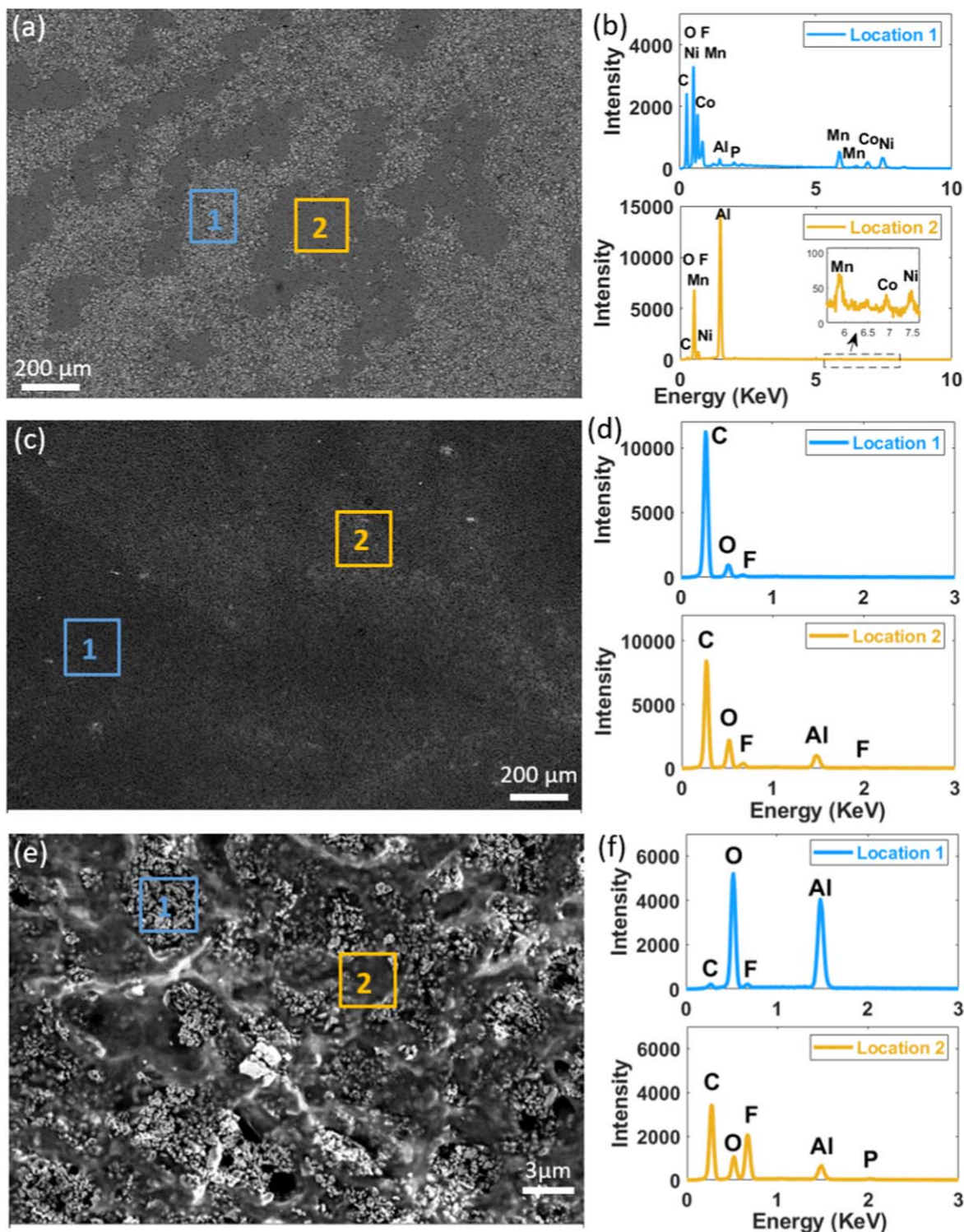


Figure 6. The surface SEM images of (a) the cathode, (c) the anode, and (e) the separator. Different locations on the SEM images were analyzed by the EDX of which the results are shown for the (b) cathode, (d), anode, and (f) separator.

coating is applied by certain manufacturers with the aim of improving the thermal characteristics of the separator and cell.^{25,26}

The microstructural details of the electrodes were investigated by analysis of the cross-sectional SEM images using the FIJI software.²⁷ Different features, i.e., active material (AM), carbon-binder domain (CBD), and porosity (POR) were identified, segmented and analyzed using a combination of plugins, as well as customized macro scripts. Multiple images from various locations were included in the analysis to ensure that the data properly represent the entire electrode (Figs. 7a, 7b).

The thickness of the cathode and anode layers were found to be 52 μm and 47 μm, respectively, closely aligning with the direct measurements using a micrometer reported earlier. The thicknesses of the aluminum and copper current collectors were determined to be 15 μm and 7.7 μm, respectively. The cathode active material particles are spherical composed of large aggregates of smaller particles, secondary particles (Fig. 7a). This is more clearly visible in the wide area distribution of the NMC particles where most of the detected segmented particles measure below 50 μm² (Fig. 7c). Note that all the AM particles below

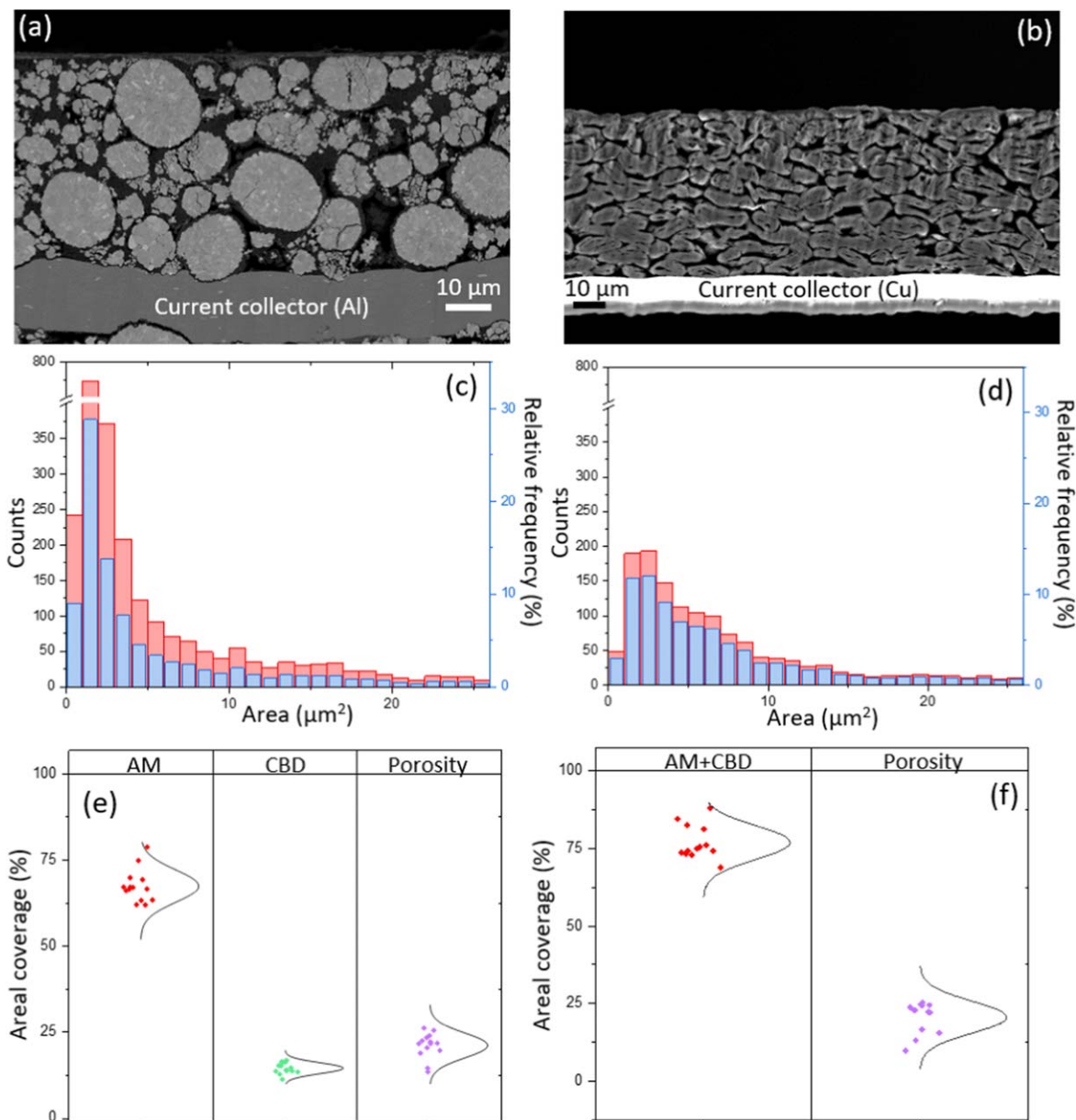


Figure 7. Typical cross-sectional SEM images of (a) cathode and (b) anode electrodes used in the image analysis. The particle area distribution determined by the image analysis is shown for (c) cathode and (d) anode. The analysis was performed on several cross-sectional SEM images of each electrode. Each data point corresponds to the average value of the respective feature in each image. (e) Areal coverage of the active material, CBD, and porosity in cathode, and (f) areal coverage of the active material + CBD, and porosity (POR) in anode.

$1 \mu\text{m}^2$ were filtered out from the histogram, since the segmentation algorithm could not distinguish gray pixels of the same value, in the CBD and AM parts. The anode active material particles exhibit a flaky morphology, primarily with particles measuring below $20 \mu\text{m}^2$ in size (Figs. 7b, 7d). In fact, these particles collectively account for 80% of the total area covered by the active material, while the larger particles constitute the remaining portion (Fig. 7d). The areal coverage of three distinct domains of AM, CBD, and porosity for the cathode and anode is shown in Figs. 7e, 7f. In these plots, each individual data point represents the data obtained from a unique cross-sectional image. The cathode features an average areal coverage of $\sim 67\%$ for AM, $\sim 13\%$ for CBD and $\sim 20\%$ for the porosity (Fig. 7e). The CBD feature was not distinguishable in the SEM images of the anode. Hence, the segmentation was done between the POR and the AM. The anode, on average, is covered by $\sim 25\%$ POR and $\sim 75\%$ by AM (Fig. 7f).

The morphological features of the electrodes were also analyzed as a function of distance from the current collector. To do so, the cross-

sectional SEM images of the electrodes were divided into 5 slices where slice number 1 and 5 represent the nearest region to the current collector and separator, respectively (Fig. 8). At the cathode, the AM tends to cover a higher area% towards the collector while the CBD tends to shrink near the current collector. This observation can be explained by the sedimentation of the larger active material particles towards the current collector and the migration of the CBD towards the electrode surface during the electrode drying process.²⁸ On the other hand, although the porosity maintains a relatively stable areal coverage, a wider variation in porosity is present at the collector's interface (Fig. 8a). At the anode, towards the collector, the AM's areal coverage gains a few percentages off that of porosity (Fig. 8b). This structural analysis indicates that there is no significant composition gradient in the cathode and anode throughout the thickness of the electrodes.

Assembling cathode and anode half-cells.—The OCV of the anode and cathode electrodes were measured inside the coin cells

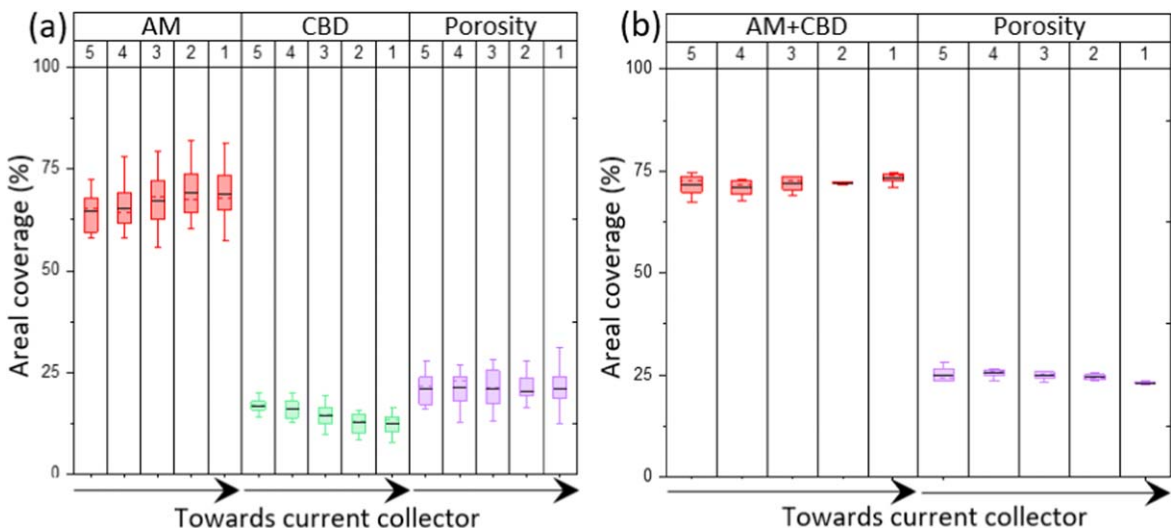


Figure 8. The areal coverage of the active material, CBD, and porosity as a function of distance from the current collector for the (a) cathode and (b) anode. At the anode, the AM and CBD are considered together as one component since the image analysis was not capable in distinguishing between the graphite particles and the carbon-binder domain. The solid horizontal lines represent the mean, while the dashed horizontal lines represent the median within the data.

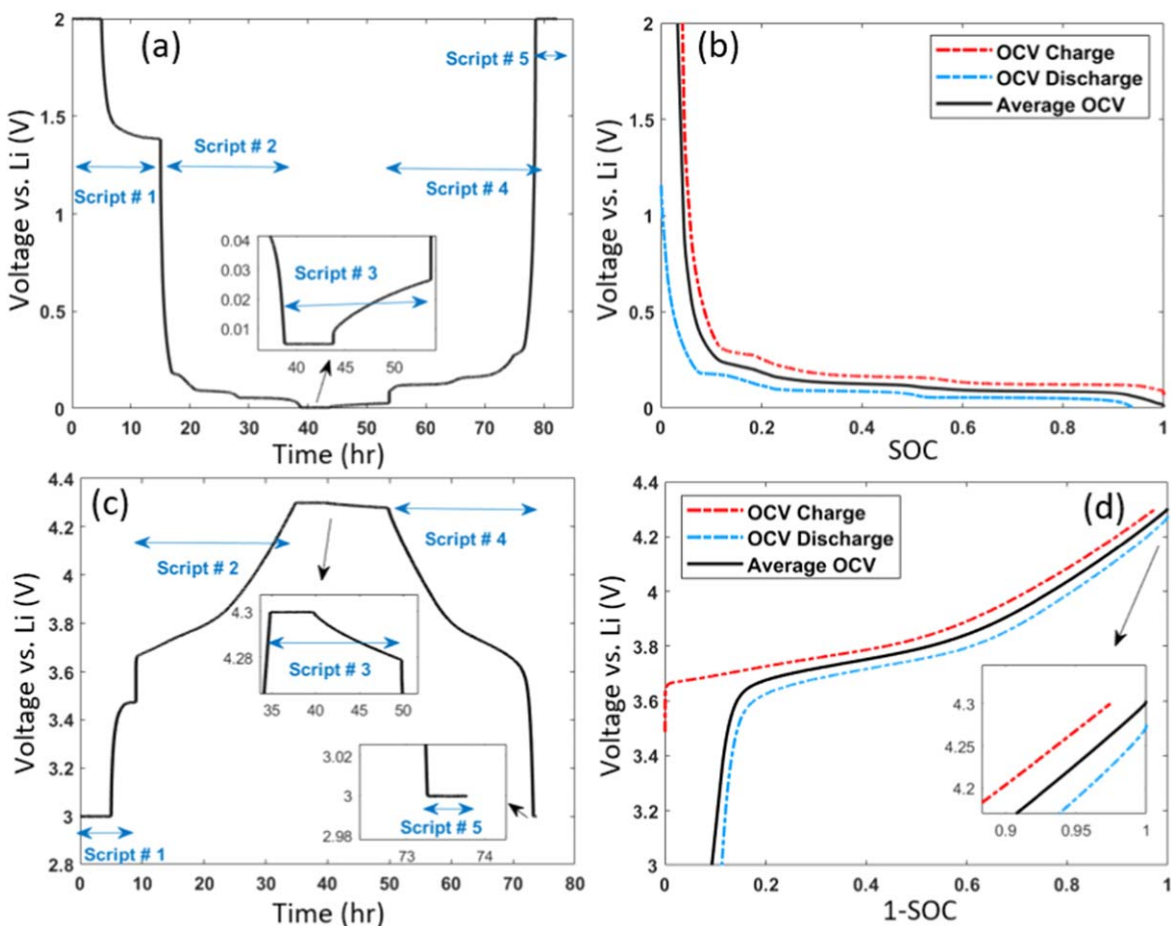


Figure 9. The unprocessed data collected from the execution of the OCV protocol outlined in the main text for the (a) anode and (c) cathode. The OCV profiles as a function of SOC for the (b) graphite and (d) NMC electrodes.

with Li counter electrode and following the same OCV test protocol earlier used for the pouch cell. The raw voltage-time data of the half-cells obtained from performing the OCV test protocol is shown for the anode and cathode half-cells in Figs. 9a and 9c, respectively. Similar to the OCV analysis of the full-cell, the SOC after script #1 is assumed to be 0 and 100% for the anode and cathode,

respectively. Similarly, the SOC after script #3 is assumed to be 100% and 0% for the anode and cathode, respectively. It is important to note that SOC refers to the state of lithiation at the anode and cathode electrodes. The voltage relaxation after the constant-voltage step is much larger in the half-cells compared to the full-cell (Figs. 9a and 9c, script #1) which results in a larger gap between

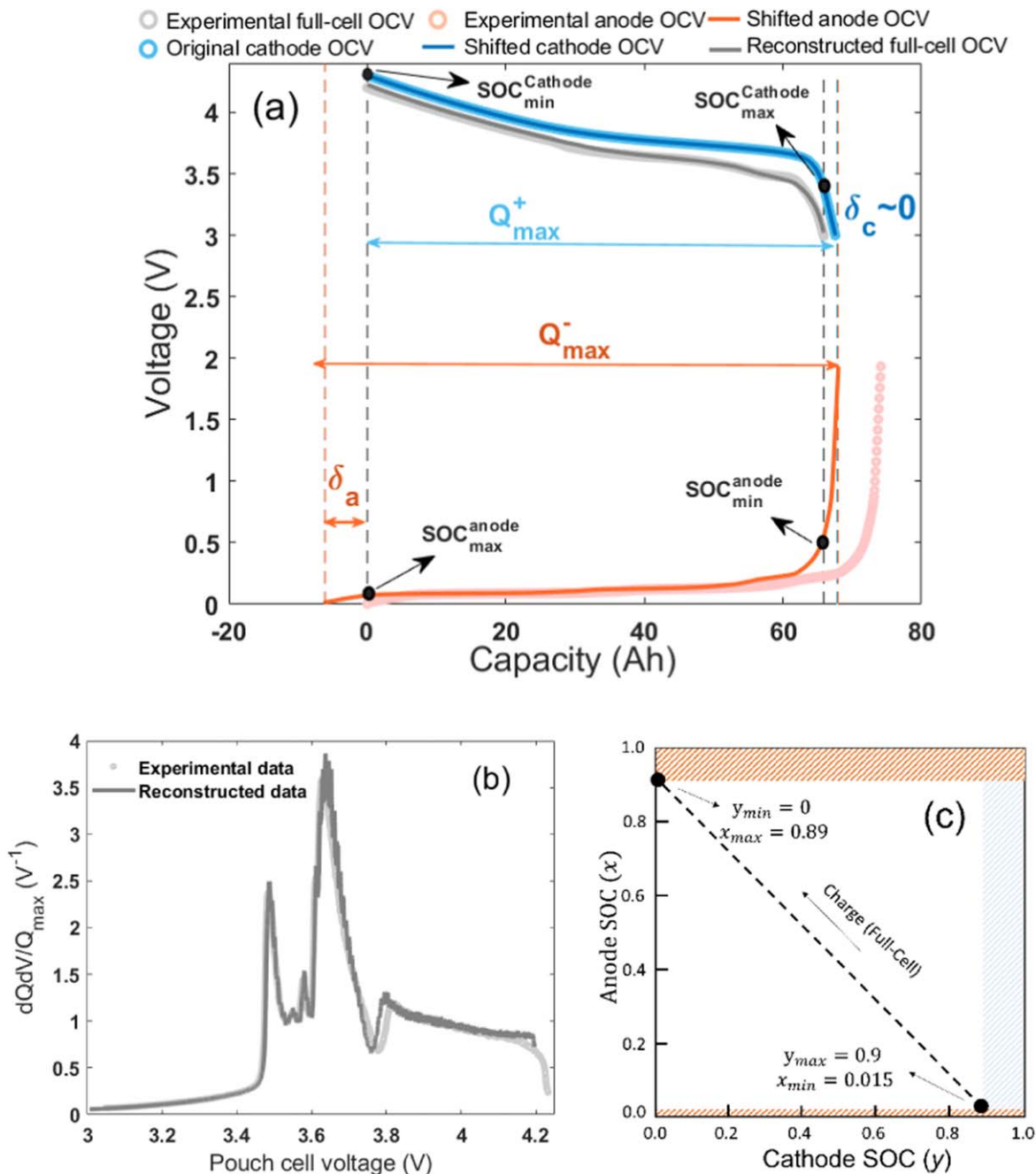


Figure 10. (a) Reconstruction of the pouch cells' OCV starting from the OCVs of the anode and cathode half cells, (b) the differential capacity signatures (dQ/dV vs voltage) of the pouch cell compared between that obtained from the experimental OCV data of the pouch cell (markers, light gray) and that reconstructed from the OCVs of the cathode and anode (dark gray), (c) the SOC cycling window of the cathode and anode electrodes within the pouch cell.

the charge and discharge OCV data near the 0 and 100% SOC, respectively. This issue is handled the same way explained for the OCV analysis of the pouch cell. The average OCVs from the processed charge and discharge OCV data are depicted in Figs. 9b and 9d for the anode and cathode, respectively.

Cell balancing.—Balancing the capacity and active-material mass between the anode and cathode of a lithium-ion cell is an important design consideration.^{29,30} An optimal cell balancing can maximize the energy density and lifetime of the cell. Particularly, in the cells with carbonaceous anodes, the continuous growth of solid-electrolyte-interphase (SEI) beyond the formation-cycle and the lithium plating phenomena accelerate upon deep lithiation of anode and at higher C-rates degrading the longevity and safety aspects of the cell.

The anode-to-cathode capacity ratio, $Z = \frac{A_a C_a}{A_c C_c}$, of the pouch cell under investigation in this study is found to be 1.03 based on the total area of the anode (A_a) and cathode (A_c) electrodes and the areal capacities of the anode (C_a) and cathode (C_c). This value of $Z > 1$ is a reasonable preventive design against aging and lithium plating. This capacity ratio is, however, smaller than a more common value of 1.1 reported in the literature.^{31,32} This suggests that the pouch cell of this study has been designed for target applications with high energy density requirements and limited power demand, i.e. lower C-rate.

The lithiation window of the anode (Δx) and cathode (Δy) within the normal operational circumstances of the pouch cell was determined using a simple mathematical model that reconstructs the OCV of the cell (\bar{U}) from those of the cathode (U_c) and anode

Table A-II. Analytical OCV functions for the graphite/Li, NMC/Li, and graphite/NMC cell based on the experimental data (Figs. 1 and 9). The functions are empirical having an arbitrary format and are aimed only at facilitating the reproduction of the experimental data.

$U_C^{\text{Charge}}(y) = -(2.1361 \times y^{12}) + (17.8490 \times y^9) - (20.5046 \times y^8)$ $+ (9.3905 \times y^5) - (4.5192 \times y^4) + (0.0362 \times y^2)$ $+ (0.3579 \times \tan(y)) + 3.6576$	0.005 < y < 0.97
$U_C^{\text{Discharge}}(y) = (1287.5582 \times y^9) - (7270.2625 \times y^8) + (17820.4708 \times y^7)$ $- (24796.4308 \times y^6) + (21494.0818 \times y^5)$ $- (11982.2700 \times y^4) + (4278.7835 \times y^3) - (941.0810 \times y^2)$ $+ (115.8807 \times y) - 2.4597$	0.113 < y < 0.99
$U_a^{\text{Charge}}(x) = -(6860.4379 \times x^9) + (34392.8119 \times x^8) - (73612.4728 \times x^7)$ $+ (87781.3044 \times x^6) - (63834.3785 \times x^5)$ $+ (29124.5019 \times x^4) - (8264.4066 \times x^3) + (1394.9837 \times x^2)$ $- (126.8854 \times x) + 5.0293$	0.043 < x < 1
$U_a^{\text{Discharge}}(x) = -(5690.2931 \times x^9) + (25655.8593 \times x^8)$ $- (48990.6895 \times x^7) + (51581.5953 \times x^6)$ $- (32673.2684 \times x^5) + (12756.5842 \times x^4)$ $- (3027.3440 \times x^3) + (415.7494 \times x^2) - (30.1577 \times x)$ $+ 1.0573$	0 < x < 0.93
$U^{\text{Charge}}(z) = (1358.1377 \times z^9) - (7283.1199 \times z^8) + (16562.8594 \times z^7)$ $- (20594.5567 \times z^6) + (14983.4659 \times z^5) - (6350.5094 \times z^4)$ $+ (1555.9431 \times z^3) - (213.3280 \times z^2) + (15.6892 \times z)$ $+ (415.8514 \times \tanh(1.5872 \times (z^{-1}))) - 412.8447$	0 < z < 0.996
$U^{\text{Discharge}}(z) = (1676.3137 \times z^9) - (8723.9040 \times z^8) + (19156.3795 \times z^7)$ $- (22896.4744 \times z^6) + (15988.0984 \times z^5)$ $- (6541.8240 \times z^4) + (1566.4563 \times z^3) - (212.9267 \times z^2)$ $+ (15.7045 \times z) + (247.0913 \times \tanh(1.4332 \times (z^{-1})))$ $- 244.1166$	0.0011 < z < 1
$U^{\text{Average}}(z) = (1512.8392 \times z^9) - (7969.0304 \times z^8) + (17757.1040 \times z^7)$ $- (21593.3835 \times z^6) + (15367.5127 \times z^5)$ $- (6401.4496 \times z^4) + (1552.5454 \times z^3) - (212.2798 \times z^2)$ $+ (15.6596 \times z) + (305.9667 \times \tanh(1.5130 \times (z^{-1})))$ $- 302.9755$	0 < z < 1

ORCID

Mohammadhosein Safari  <https://orcid.org/0000-0003-0633-731X>

References

1. M. Li, J. Lu, Z. Chen, and K. Amine, *Adv. Mater.*, **30**, 1800561 (2018).
2. R. Schröder, M. Aydemir, and G. Seliger, *Procedia Manufacturing*, **8**, 104 (2017).
3. A. Kwade, W. Haselrieder, R. Leithoff, A. Modlinger, F. Dietrich, and K. Droeder, *Nat. Energy*, **3**, 290 (2018).
4. F. Günter and N. Wassiliadis, *J. Electrochem. Soc.*, **169**, 030515 (2022).
5. L. Wildfeuer, N. Wassiliadis, A. Karger, F. Bauer, and M. Lienkamp, *Journal of Energy Storage*, **48**, 103909 (2022).
6. S. Tamilselvi, S. Gunasundari, N. Karupiah, A. Razak RK, S. Madhusudan, V. M. Nagarajan, T. Sathish, M. Z. M. Shamim, C. A. Saleel, and A. Afzal, *Sustainability*, **13**, 10042 (2021).
7. J. Le Houx and D. Kramer, *Energy Reports*, **6**, 1 (2020).
8. N. Jin, D. L. Danilov, P. M. Van den Hof, and M. Donkers, *Int. J. Energy Res.*, **42**, 2417 (2018).
9. J. C. Forman, S. J. Moura, J. L. Stein, and H. K. Fathy, *Proceedings of the 2011 American Control Conference (IEEE)*, p. 362 (2011).
10. L. Zhang, L. Wang, G. Hinds, C. Lyu, J. Zheng, and J. Li, *J. Power Sources*, **270**, 367 (2014).
11. E. Namor, D. Torregrossa, R. Cherkaoui, and M. Paolone, *Journal of Energy Storage*, **12**, 138 (2017).
12. J. Marcicki, M. Canova, A. T. Conlisk, and G. Rizzoni, *J. Power Sources*, **237**, 310 (2013).
13. C.-H. Chen, F. B. Planella, K. O'regan, D. Gastol, W. D. Widanage, and E. Kendrick, *J. Electrochem. Soc.*, **167**, 080534 (2020).
14. S. Lee, J. B. Siegel, A. G. Stefanopoulou, J.-W. Lee, and T.-K. Lee, *J. Electrochem. Soc.*, **167**, 090531 (2020).
15. G. L. Plett, *Battery Management Systems, Volume I: Battery modeling* (Artech House) (2015).
16. D. Lu, M. S. Trimboli, G. Fan, R. Zhang, and G. L. Plett, *J. Electrochem. Soc.*, **168**, 070532 (2021).
17. R. Amin and Y.-M. Chiang, *J. Electrochem. Soc.*, **163**, A1512 (2016).
18. D. M. Bernardi and J.-Y. Go, *J. Power Sources*, **196**, 412 (2011).
19. J. Landesfeind and H. A. Gasteiger, *J. Electrochem. Soc.*, **166**, A3079 (2019).
20. E. Logan, E. M. Tonita, K. Gering, L. Ma, M. K. Bauer, J. Li, L. Beaulieu, and J. Dahn, *J. Electrochem. Soc.*, **165**, A705 (2018).
21. T. Teuffl, D. Pritzl, S. Solchenbach, H. A. Gasteiger, and M. A. Mendez, *J. Electrochem. Soc.*, **166**, A1275 (2019).
22. H. Hamed, S. Yari, J. D'Haen, F. U. Renner, N. Reddy, A. Hardy, and M. Safari, *Adv. Energy Mater.*, **10**, 2002492 (2020).
23. H. Hamed, L. Henderick, B. G. Choobar, J. D'Haen, C. Detavernier, A. Hardy, and M. Safari, *Science*, **24**, 103496 (2021).
24. S. Ludwig, I. Zilberman, M. F. Horsche, T. Wohlers, and A. Jossen, *J. Power Sources*, **490**, 229523 (2021).
25. G. Sharma, Y. Jin, and Y. Lin, *J. Electrochem. Soc.*, **164**, A1184 (2017).
26. G. Kovachev, H. Schröttner, G. Gstrein, L. Aiello, I. Hanzu, H. M. R. Wilkening, A. Foitzik, M. Wellm, W. Sinz, and C. Ellersdorfer, *Batteries*, **5**, 67 (2019).
27. J. Schindelin, I. Arganda-Carreras, E. Frise, V. Kaynig, M. Longair, T. Pietzsch, S. Preibisch, C. Rueden, S. Saalfeld, and B. Schmid, *Nat. Methods*, **9**, 676 (2012).
28. S. Jaiser, M. Müller, M. Baunach, W. Bauer, P. Scharfer, and W. Schabel, *J. Power Sources*, **318**, 210 (2016).
29. J. Christensen and J. Newman, *J. Electrochem. Soc.*, **152**, A818 (2005).
30. J. Kasnatscheew, T. Placke, B. Streipert, S. Rothermel, R. Wagner, P. Meister, I. C. Laskovic, and M. Winter, *J. Electrochem. Soc.*, **164**, A2479 (2017).
31. Y. Abe and S. Kumagai, *Journal of Energy Storage*, **19**, 96 (2018).
32. B. F. Song, A. Dhanabalan, and S. L. Biswal, *Journal of Energy Storage*, **28**, 101268 (2020).
33. S.-C. Yin, Y.-H. Rho, I. Swainson, and L. Nazar, *Chem. Mater.*, **18**, 1901 (2006).

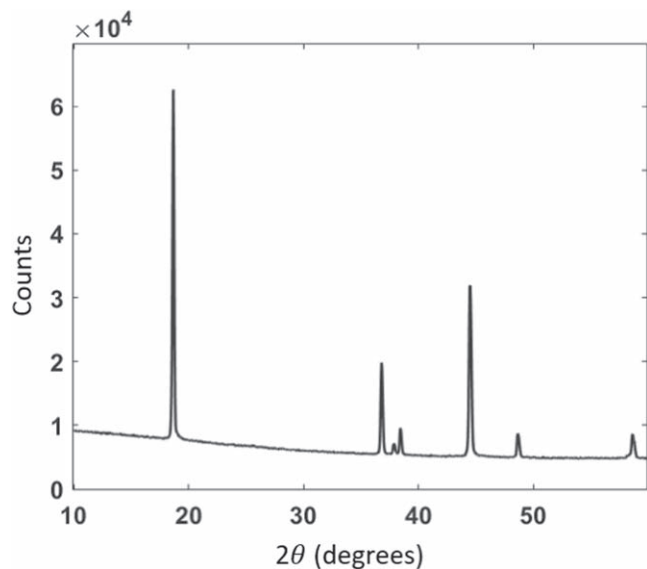


Figure A-1. XRD patterns of NMC electrode harvested from a fully discharged pouch cell. Comparison to the data reported by Yin et al.³³ shows that the composition of the NMC in our work is $\text{LiNi}_{0.33}\text{Mn}_{0.33}\text{Co}_{0.33}$. The parameters obtained from this XRD analysis are outlined in table A1. $\text{WL} = 1.5406 \text{ \AA}$.

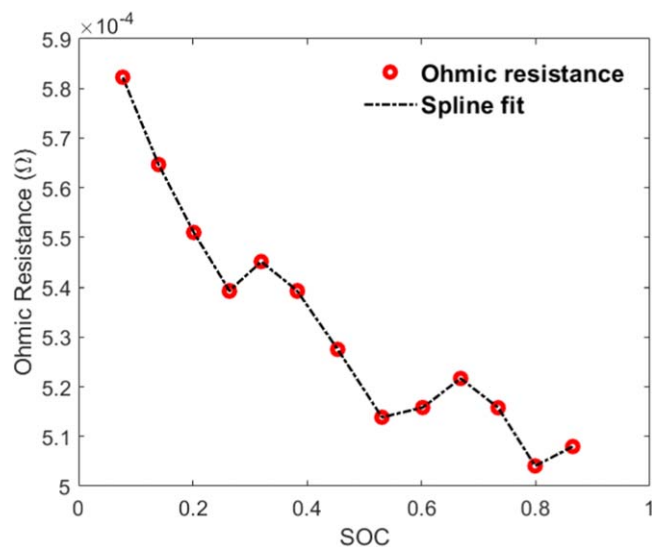


Figure A-2. The ohmic resistance as a function of SOC obtained from a pulse-relaxation test performed on a fully charged pouch cell at 25 °C. 0.8 C current pulses were applied for 5 min and then the current was interrupted. The ohmic resistance was calculated following the same method described in the resistance and rate capability section. The ohmic resistance values are close to those obtained from the pulse-relaxation test with 0.2 C current pulses (Fig. 2b).